Materials Horizons

ROYAL SOCIETY OF CHEMISTRY

COMMUNICATION

View Article Online
View Journal | View Issue

Cite this: *Mater. Horiz.*, 2025, **12**, 5342

Received 6th January 2025,
Accepted 25th March 2025

DOI: 10.1039/d5mh00023h

rsc.li/materials-horizons

The van der Waals antiferromagnetic proximity effect at the $FePS_3$/Pt uncompensated interface†

Yinchang Ma, ‡[a] Shijie Xu,‡[a] Zhuo Chen,[a] Chen Liu,[a] Tao Yang,[a] Yuan Yan,[b] Jefferson Zhe Liu,[b] Fei Xue[cd] and Xixiang Zhang *[a]

van der Waals antiferromagnetic insulators are emerging as promising candidates for spintronics and quantum computing due to their unique magnetic properties. However, detecting antiferromagnetism at the atomic scale remains challenging due to compensated spin order. In this study, we present a novel approach to observe the antiferromagnetic proximity effect in $FePS_3$/Pt heterostructures. This effect arises from interfacial magnetic moments, which induce significant spin polarization in the Pt layer *via* strong interlayer exchange interactions. As a result, a pronounced anomalous Hall effect is observed in the Pt layer. Fe atom vacancies at the $FePS_3$/Pt interface play a critical role in creating localized surface magnetic moments and enhancing exchange interactions. These findings shed light on the complex interplay between two-dimensional antiferromagnetic insulators and heavy metals with strong spin–orbit coupling, providing a promising strategy to exploit interfacial effects for creating magnetization in antiferromagnetic materials.

New concepts

Low-dimensional magnetic materials, particularly antiferromagnetic insulators, hold great promise for spintronic applications but present challenges in detecting and manipulating magnetization at the atomic scale due to their lack of net magnetic moment. To address this, we studied $FePS_3$/Pt heterostructures and proposed a novel approach to induce and detect magnetization in antiferromagnetic insulator/heavy metal systems. Our study demonstrates the antiferromagnetic proximity effect, where Pt exhibits magnetization despite the net-zero magnetic moment of $FePS_3$ in its bulk state. Besides, we show that Fe atom vacancies at the interface induce local net magnetic moments and enhance interfacial exchange interactions, providing a pathway for magnetization creation. Using a defect model, we elucidate the van der Waals antiferromagnetic proximity effect, offering insights into the interplay between magnetic proximity effects, defect engineering, and interfacial interactions. These findings present universal strategies to induce net magnetization in metals with strong spin–orbit coupling for spintronic applications in low-dimensional systems.

Introduction

van der Waals magnetic materials have attracted attention for their potential applications in spintronics,[1–5] quantum computing,[6] and other advanced technologies.[7–12] van der Waals antiferromagnetic insulators, in particular, possess unique magnetic properties, such as ultrafast dynamics, zero stray fields, and diverse spin configurations.[13–15] As a van der Waals antiferromagnetic insulator, $FePS_3$ exhibits robust exchange interactions and strong magnetic anisotropy,[14,16] making it a compelling platform for studying magnetic phenomena in two-dimensional (2D) systems. However, detecting and manipulating the magnetization of these materials at the atomic scale are challenging. Antiferromagnetic ordering in $FePS_3$ leads to a zero net magnetic moment, making the traditional magnetization detection techniques ineffective.[17]

Interfacial magnetic interactions provide opportunities for advancing the detection and manipulation of magnetism at the nanoscale. When a magnetic material is in contact with a heavy metal with strong spin–orbit coupling, a novel magnetic effect can arise due to interfacial interactions.[18–20] This effect, known as the magnetic proximity effect (MPE),[21–26] has attracted significant research interest in the field of van der Waals materials and heterostructures due to its potential to induce various magneto-transport phenomena such as the spin valve effect,[27] quantum anomalous Hall effect,[28] and spin–valley coupling.[29]

Recent studies of the MPE in 2D materials have revealed a variety of mechanisms, significantly enhancing our understanding of this phenomenon.[30] Zollner *et al.*[31] investigated the MPE

[a] *Physical Science and Engineering Division, King Abdullah University of Science and Technology, Thuwal 23955, Saudi Arabia. E-mail: xixiang.zhang@kaust.edu.sa*
[b] *Department of Mechanical Engineering, The University of Melbourne, Parkville, VIC, 3010, Australia*
[c] *Center for Quantum Matter, School of Physics, Zhejiang University, Hangzhou 310027, China*
[d] *ZJU-Hangzhou Global Scientific and Technological Innovation Center, Zhejiang University, Hangzhou, 311215, China*

† Electronic supplementary information (ESI) available. See DOI: https://doi.org/10.1039/d5mh00023h

‡ Contributed equally.

in graphene/transition-metal phosphorus trichalcogenide (MPX_3; M = Mn, Fe, Ni, Co; X = S, Se) heterostructures. Through first-principles calculations, they demonstrated the induction of sizable magnetization in graphene. Zhong *et al.*[32] and Lyons[33] *et al.* in 2020 explored the MPE in transition metal dichalcogenide (TMD)/ferromagnet heterostructures, showing that a strong exchange field and spin–orbit coupling can be induced in TMDs such as WSe_2 and $MoSe_2$. These studies create enhanced spin-polarized electronic states for novel spintronic devices.

Shi *et al.*[18,20,34,35] have made significant contributions to leveraging the MPE for detecting nanoscale magnetism. Their studies demonstrated that the magnetic properties of 2D magnetic insulators could be effectively probed through the anomalous Hall effect (AHE) of adjacent metals.[20,25,36,37] However, most existing studies focus on 2D ferromagnetic materials such as $Cr_2Ge_2Te_6$[20] and $CrBr_3$.[21] Investigations into 2D antiferromagnetic insulators using the MPE remain scarce. In this work, we report the AHE in antiferromagnetic $FePS_3$/Pt heterostructures. Despite the absence of net magnetic moment in $FePS_3$, the AHE was detected in the Pt layer, suggesting the emergence of net magnetization in the Pt layer. This phenomenon is primarily attributed to the MPE; specifically, the antiferromagnetic order in $FePS_3$ influences the Pt layer *via* strong interlayer exchange coupling.[18,19] Supported by first-principles calculations, we point out the potential role of Fe atom vacancies in introducing local magnetic moments and enhancing the exchange interactions at the $FePS_3$/Pt interface, thereby amplifying the MPE.[38] A series of transport measurements reveal that interfacial physics influences the magnetic properties and transport behaviors in the heterostructures.

Results and discussion

The structural, compositional, and magnetic characterization of bulk $FePS_3$ is presented in Fig. 1. The photograph of the $FePS_3$ bulk crystal is shown in the inset of Fig. 1a. The Raman spectrum displays the characteristic vibrational modes of $FePS_3$ (Fig. 1a). The Raman peaks correspond to the in-plane phonon modes of the E_g and E_u types and out-of-plane modes of the A_{1g} type, all originating from the vibration of $[P_2S_6]^{4-}$ units.[39] Elemental analysis *via* energy-dispersive X-ray spectroscopy (EDS) (Fig. 1b, top panel) confirms the stoichiometric composition of $FePS_3$. The atomic percentage of Fe is 19.57%, close to the theoretical stoichiometry and is within the acceptable error range of the instrument. The X-ray diffraction (XRD) pattern (Fig. 1b, bottom panel) validates the crystalline structure of $FePS_3$, with sharp peaks corresponding to (001), (002), (003), and (004) crystal planes, confirming the high crystallinity. The magnetization curves (Fig. 1c and d) clearly demonstrate the antiferromagnetic nature of $FePS_3$. The magnetization *versus* temperature (*M*–*T*) curves measured at 1000 Oe show clear antiferromagnetic–paramagnetic transitions and confirm the Néel temperature to be around 118 K (Fig. 1d). The magnetization *versus* applied magnetic field (*M*–*H*) curves (Fig. 1c) confirm the characteristics of an antiferromagnet with strong anisotropy.

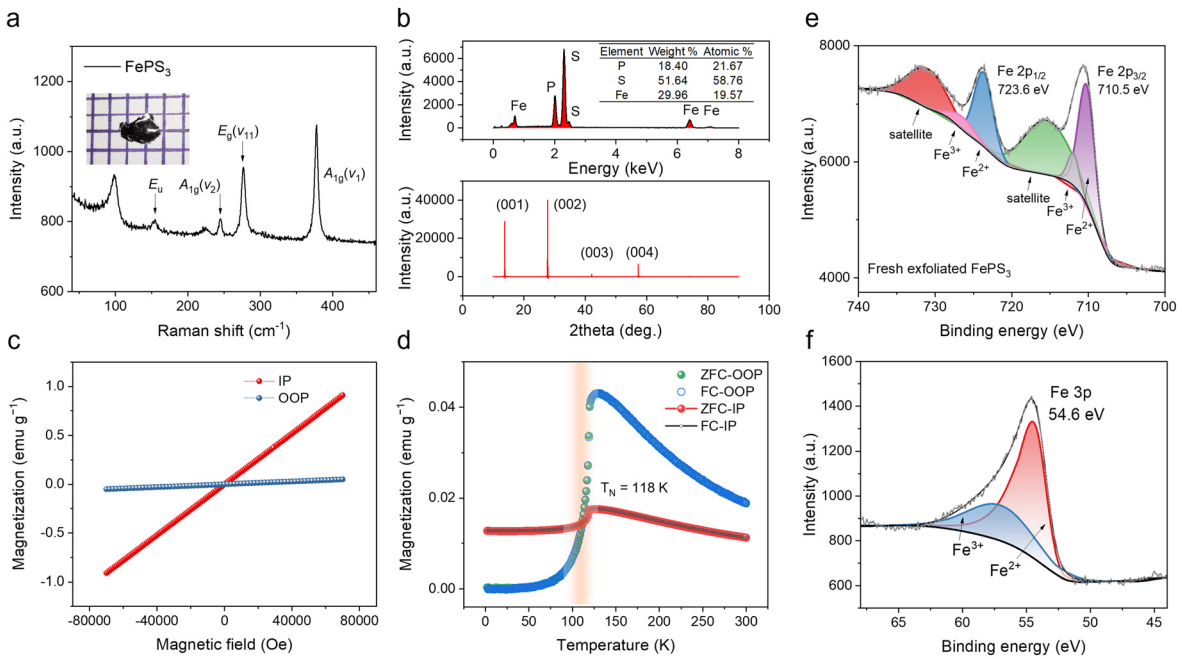

Fig. 1 Structural, compositional and magnetic characterization of $FePS_3$ bulk crystals. (a) Raman spectrum showing the characteristic peaks of $FePS_3$. Inset: Photograph of the $FePS_3$ bulk crystal. Grid size: 1 mm × 1 mm. (b) Top panel: Elemental analysis of $FePS_3$ using EDS and a table listing the weight percentages and atomic percentages of P, S, and Fe. Bottom panel: XRD pattern of $FePS_3$. (c) Magnetization–field curves of bulk $FePS_3$. (d) Magnetization–temperature curves of bulk $FePS_3$ measured under 1000 Oe. IP and OOP in (c) and (d) refer to in-plane and out-of-plane, respectively. (e) XPS spectra of Fe 2p peaks for exfoliated few-layer $FePS_3$ crystals. (f) XPS of Fe 3p peaks for few-layer $FePS_3$.

The perfect linear response with the field perpendicular to the Néel vector persisting up to 7 T indicates the non-canting nature of the antiferromagnetic alignment of spins with near-zero net moment. It is also evident that the Néel vector is parallel to the *c*-axis, *i.e.*, there is a perpendicular magnetic anisotropy.

To investigate the structural and electronic properties of $FePS_3$ in two dimensions, the as-grown bulk crystal was mechanically exfoliated into few-layer flakes. XPS measurements of freshly exfoliated $FePS_3$ flakes reveal the coexistence of Fe^{2+} and Fe^{3+} valence states (Fig. 1e and f), which are attributed to vacancies rather than oxidation, as the samples were transferred to a high-vacuum chamber immediately after exfoliation to exclude surface oxidation. Quantitative analysis of XPS data is shown in Tables S1 and S2 (ESI†). Transmission electron microscopy confirms the existence of Fe vacancies in exfoliated ultra-thin (6-nm) $FePS_3$ samples (Fig. S1, ESI†). The Fe vacancies could alter coordination environments on the surface of exfoliated flakes. Such a significant change of the surface state is also evident from the blue-shifted Raman characteristic peaks after exfoliation (top panel of Fig. S2, ESI†). The blue shift of the Raman peaks is a feature of lattice compression because a small lattice constant corresponds to a higher phonon frequency and a larger Raman shift. The bottom panel of Fig. S2 (ESI†) illustrates how a vacancy induces local lattice distortions. The neighboring atoms are distorted around the vacancy. Both compressive strain and local bond stiffening are reasons for Raman blue shifts.

The possible effect of these surface states on the nanoscale magnetic properties cannot be directly detected using a superconducting quantum interference device (SQUID) magnetometer. Therefore, to investigate the elusive magnetization in few-layer $FePS_3$, the exfoliated few-layer flakes were fabricated into $FePS_3$/Pt Hall bar devices for magneto-transport measurements. Fig. 2 displays the structure of the $FePS_3$/Pt heterostructures. The 3D schematic and optical microscopy image (Fig. 2a) display the fabricated Hall bar device constructed from an $FePS_3$ (20 nm)/Pt (6 nm) heterostructure. Fig. 2b depicts the MPE at the interface between a heavy metal and a magnetic material.[40] Magnetic ordering in the magnetic material induces spin polarization in the adjacent metal layer. In this study, Pt is chosen primarily because of its high susceptibility to magnetic influence. Specifically, it provides strong spin–orbit coupling and considerable exchange energy, bringing it close to satisfying the Stoner criterion: $(I_E \cdot DOS(E_F) > 1$, where I_E is the exchange integral and $DOS(E_F)$ is the density of states at the Fermi level).[41] The Stoner criterion indicates the tendency of a material to become ferromagnetic based on the balance between the exchange interaction energy and the kinetic energy of the conduction electrons. Pt, while not ferromagnetic in bulk form, has a large $DOS(E_F)$ and a large I_E that bring it close to meeting the

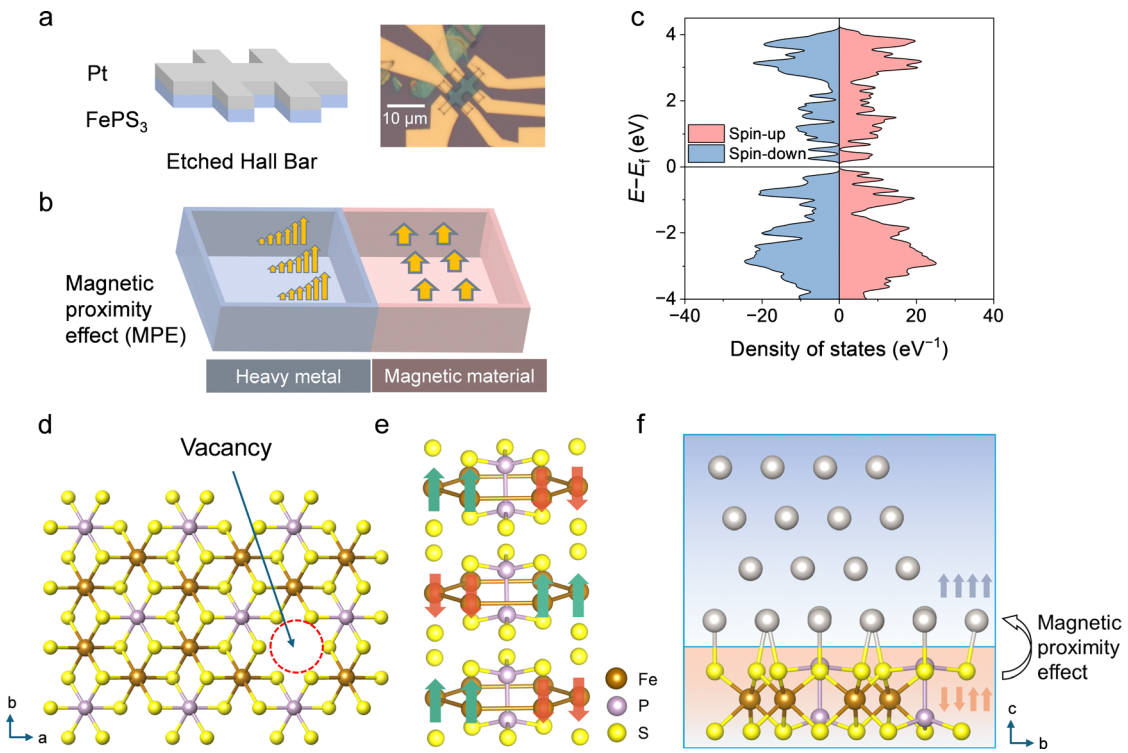

Fig. 2 Device fabrication and structure details of $FePS_3$/Pt heterostructure. (a) Left panel: schematic of the etched Hall bar composed of exfoliated $FePS_3$ and sputtered Pt. Right panel: optical microscope image of the fabricated Hall bar device based on an $FePS_3$ (20 nm)/Pt (6 nm) heterostructure. Scale bar: 10 μm. (b) Schematic of the MPE-induced magnetization distribution at the interface of a heavy metal and a magnetic material, with arrows indicating the direction of spin polarization. (c) Calculated spin DOS as a function of energy for $FePS_3$ with Fe vacancies. (d) $FePS_3$ crystal structure with an Fe vacancy, predicted by DFT calculations. (e) Crystal structure of $FePS_3$ with antiferromagnetic order (indicated by arrows) along the *c*-axis. (f) Schematic of DFT-predicted atomic structure of the $FePS_3$/Pt interface. Interfacial magnetic ordering in $FePS_3$ induces spin polarization in the proximate Pt layer.

Stoner criterion. This implies that even a slight magnetization from an adjacent magnetic material can convert Pt into a magnetic state. Proximity-induced spin polarization in Pt is a key for understanding the magnetic order in few-layer $FePS_3$ and elucidating the origin of the AHE observed in this work.

Fig. 2e shows the layered stacking of $FePS_3$ along the *c*-axis, with inherent antiferromagnetic ordering reported in previous studies.[13,42] The magnetic moments of the Fe atoms are aligned in antiparallel directions both within the same plane and between the layers, suggesting both interlayer and intralayer antiferromagnetic coupling. Removal of an Fe atom can disrupt the periodic lattice arrangement and long-distance magnetic exchange interactions, affecting the spin compensation of Fe atoms (Fig. 2d). This can create magnetic moments, modify localized magnetic interactions and potentially alter the type of magnetic order. In $FePS_3$/Pt heterostructures, Fe vacancies can induce ferromagnetic-like order at the interface, leading to spin polarization in the Pt layer and pronounced spin-dependent transport properties through the MPE (Fig. 2f). Understanding this vacancy-induced magnetization is crucial for optimizing $FePS_3$ and other 2D antiferromagnets in spintronic applications, because such vacancies can be exploited to achieve the desired magnetic properties. Fig. 2c presents the calculated spin density of states in the predicted defective $FePS_3$. The spin-up and spin-down states are asymmetric near the Fermi level, indicating net spin polarization. Fig. S3 (ESI†) presents the spin charge density distribution in the defective $FePS_3$ structure. The noticeable imbalance between the spin-up and spin-down densities suggests net magnetization. These first-principles calculations reveal the electronic structural modifications at the interface, which is a prerequisite for explaining the subsequent magneto-transport measurement results.

The electric measurements of the $FePS_3$/Pt heterostructure were conducted to elucidate the interfacial coupling through magneto-transport characteristics (Fig. 3). The decrease in longitudinal resistance (R_{xx}) with increasing temperature (Fig. S4, ESI†) shows a typical characteristic of metallic conductors, indicating that the Pt layer dominates the transport properties. The transverse resistance (R_{xy}) *versus* magnetic field plots at various temperatures (Fig. 3a) strongly support the presence of the AHE in the Pt layer. The abrupt change of R_{xy} near zero field indicates the contribution of the anomalous Hall resistance. R_{xy} saturating at ± 2 T indicates the saturation field. The AHE is most pronounced at 2 K (the lowest investigated temperature). The anomalous Hall resistance is expressed as $R_{AHE} = (R_{xy+} - R_{xy-})/2$, where R_{xy+} and R_{xy-} are the R_{xy} values extrapolated from the maximum positive and negative magnetic fields to zero magnetic field.[43] Fig. 3b and c shows the evolution of the anomalous Hall resistance with temperature. The AHE resistance decreases with increasing temperature, finally reversing the sign above 100 K (Fig. 3d). This transition temperature agrees with the measured T_N in Fig. 1d, showing consistency between the AHE resistance and magnetization. This consistency suggests that the induced magnetization in the Pt layer is responsible for the observed AHE. The R_{AHE}–H relation approaches linearity as the temperature rises above 140 K (Fig. S5d, ESI†), suggesting that the induced magnetization in Pt weakens at higher temperatures. The temperature sensitivity of the AHE indicates that the proximity-induced spin polarization in Pt is associated with the magnetization in $FePS_3$. A contrast experiment was conducted by inserting a 4 nm Cu layer between the

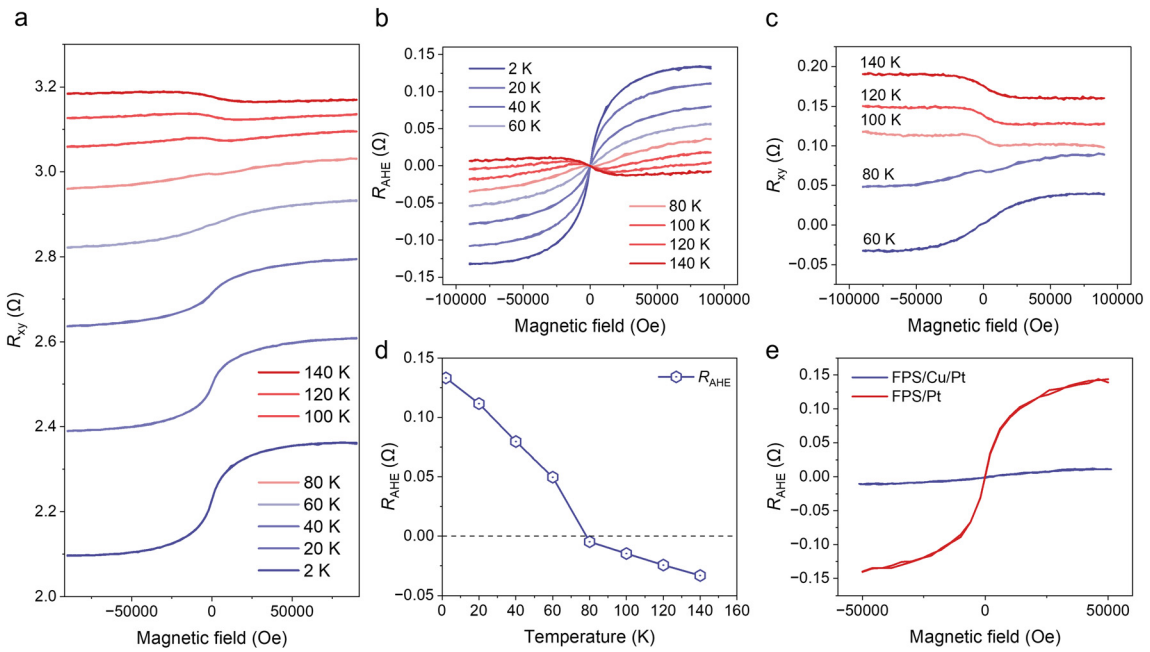

Fig. 3 Magneto-transport measurements of $FePS_3$/Pt heterostructures. (a) R_{xy} *versus* magnetic fields from −9 T to 9 T at various temperatures. The field is applied OOP. (b) R_{AHE} *versus* magnetic fields at various temperatures. (c) R_{AHE} *versus* magnetic field showing the sign reversal of the Hall resistance near 100 K. (d) Temperature dependence of R_{AHE}. (e) Comparison of R_{AHE} between $FePS_3$/Pt and $FePS_3$/Cu/Pt heterostructures.

$FePS_3$ and Pt layers. The $FePS_3$/Cu/Pt heterostructure shows an almost vanished AHE signal compared to $FePS_3$/Pt, confirming that the observed AHE originates from the proximity effect (Fig. 3e).

To understand the underlying mechanisms of the observed AHE, Fig. 4 schematically depicts the MPE and the induced magnetization in the $FePS_3$/Pt heterostructure. The non-defective state (Fig. 4a) shows $FePS_3$ with its antiferromagnetic ordering and Pt as a non-magnetic material. The antiferromagnetic order in pristine $FePS_3$ is represented by antiparallel spin pairs that produce zero net magnetization. As Pt is non-magnetic, it does not exhibit any intrinsic magnetic order when it is far away from the magnetic layer. Fig. 4b presents the induction of net magnetization in the Pt layer caused by the MPE at the $FePS_3$/Pt interface, where the thin $FePS_3$ flake contains Fe vacancies. When $FePS_3$ and Pt are brought into close contact, the magnetic order of $FePS_3$ influences the Pt layer, causing a large spin polarization. The spins align toward the applied magnetic field orientation. This induced spin polarization is a direct consequence of the interfacial exchange interactions between the net moments of the vacancies in the antiferromagnetic $FePS_3$ and the adjacent Pt. The contribution of the vacancy is crucial for understanding the generation of ferromagnetism in this antiferromagnet/heavy metal system. The introduction of Fe atom vacancy in $FePS_3$ can create local magnetic moments that disrupt the perfect antiferromagnetic order, serving as an effective medium for localized short-distance ferromagnetic exchange coupling. These vacancies enhance the exchange interactions at the $FePS_3$/Pt interface, strengthening the induced magnetization in the Pt layer. The local magnetic moments generated by these vacancies are estimated as $3.3\mu_B$ per vacancy based on our DFT calculations and the literature.[44–51] Fig. 4c depicts the spin orientation in the heterostructure under a downward magnetic field. The reversal of magnetic moment alignment in Pt, induced by the downward field, demonstrates the effective moments of vacancies and the switchable polarity of the MPE in response to an external field.

While the proximity-induced AHE is evident, whether it can persist at minimized thickness is still an open question. To explore the size effect, the thickness of $FePS_3$ in the heterostructure was decreased to 8 nm. At this reduced thickness, the AHE remains evident. The loops diminish with increasing temperature, and the inversion of the AHE signal is clearly observed around 100 K (Fig. S5a and d, ESI†). Moreover, the variation of AHE resistance with temperature (Fig. S5b and c, ESI†) shows that AHE resistance exhibits a large value at low temperature, consistent with the weakening of the MPE at higher temperatures as the thermal energy overcomes the exchange interactions at the $FePS_3$/Pt interface, thereby reducing the induced magnetization.

The observed AHE inversion can be attributed to several possible factors: (1) competing magnetic interactions;[52] (2) competition between spin Hall magnetoresistance (SMR) and MPE-induced anomalous Hall conductivity;[53–55] (3) thermal activation of defects;[56,57] and (4) spin reorientation transition.[58] There could be competition between different magnetic interactions across the interface or between multiple co-existing magnetic phases in the heterostructure. As the temperature increases, the balance between them might shift, leading to a change in the direction of induced spin polarization. Competition between the SMR-induced AHE and the proximity-induced AHE provides another explanation for the observed sign reversal of the AHE. Different from the origin of the AHE, SMR arises from the interactions between the spin-polarized currents and the magnetic moments on top surface of $FePS_3$, where the orientation and magnitude of the magnetization affect the resistance experienced by spin currents. The dynamic interplay between these two mechanisms can lead to variations in the sign of R_{AHE}, depending on which mechanism is dominant under different magnetic field strengths and temperatures.

To investigate SMR and anisotropic magnetoresistance (AMR), the angular dependence of R_{xx} was obtained (Fig. 5 and Fig. S6,

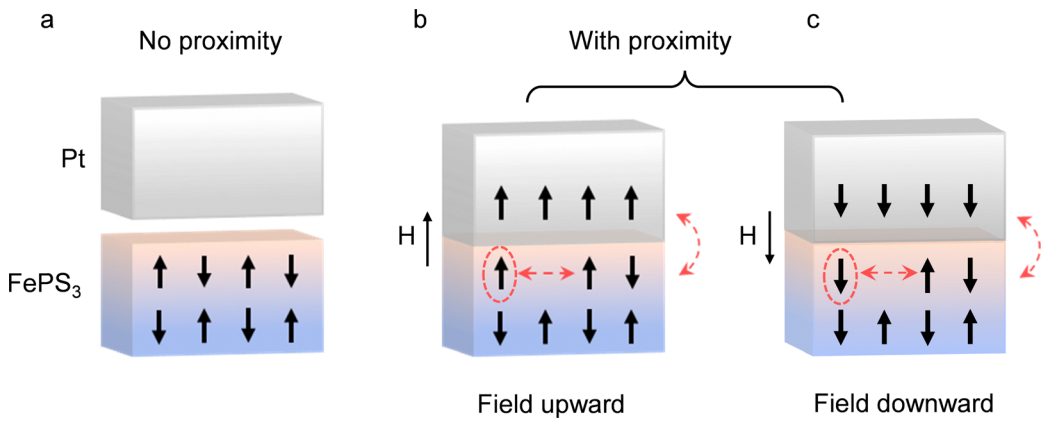

Fig. 4 Schematics of magnetic proximity effect and induced magnetization in $FePS_3$/Pt heterostructures. (a) Initial state, in which $FePS_3$ is antiferromagnetically ordered and Pt is non-magnetic. (b) Emergence of net magnetization in the Pt layer due to the MPE at the $FePS_3$/Pt interface, where the ferromagnetic order mediated by Fe atom vacancy in $FePS_3$ influences the Pt layer, causing spin polarization. The net magnetization in $FePS_3$ and Pt aligns toward the external magnetic field orientation. (c) Spin configuration with proximity effect and a downward magnetic field. The net moments are marked by circles.

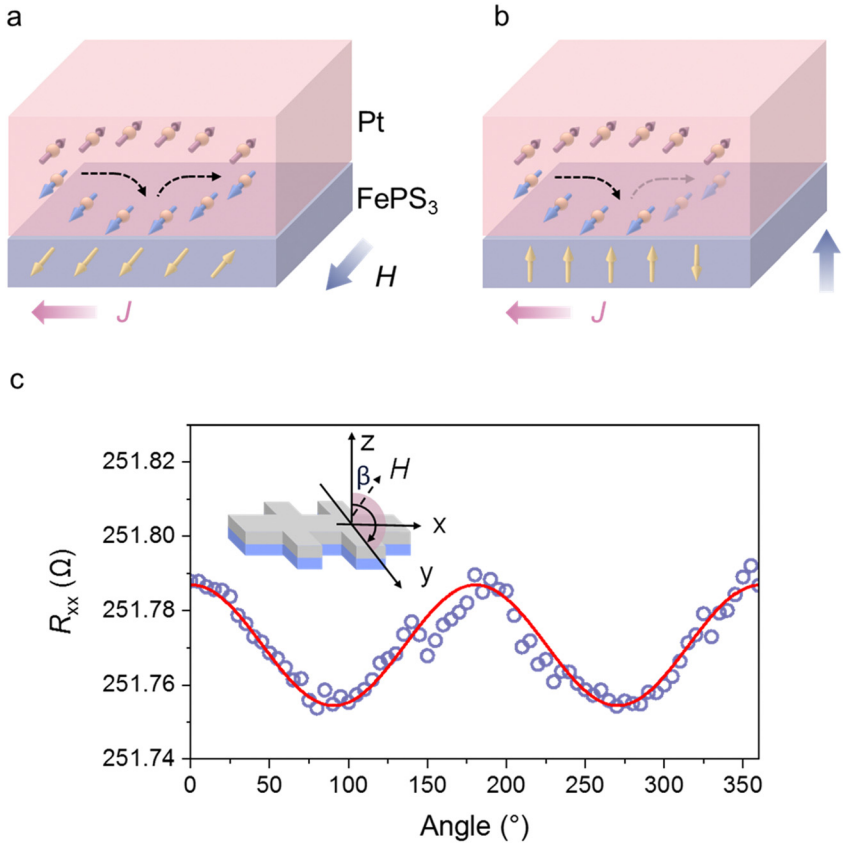

Fig. 5 SMR measurements of $FePS_3$/Pt heterostructure. (a) Schematics of the SMR mechanism, where a spin current is generated in the Pt layer due to an applied current and spin Hall effect. When the magnetic field aligns the magnetization in $FePS_3$ parallel to the spin direction of spin current in Pt, the spin current is reflected at the interface, resulting in low resistance. (b) When the applied field drives the magnetization in $FePS_3$ perpendicular to the spin direction of spin current in Pt, the spin current is absorbed by $FePS_3$, leading to an increase in resistance. (c) Angular dependence of the longitudinal resistance R_{xx} as a function of the angle between the external magnetic field and the z-axis. The inset illustrates the experimental setup. The field rotates in y–z plane.

S7, ESI†). Fig. 5 schematically illustrates how the spin current behavior in Pt is influenced by the surface magnetic state of $FePS_3$. Fig. S6a and S7a (ESI†) illustrate the measurement setup, where the applied magnetic field rotates in the x–z plane and y–z plane, respectively, with the rotation angle (β and γ, respectively) varying from 0° to 360°. The observed sinusoidal variation in R_{xx} confirms the SMR (Fig. 5c) and AMR effects (Fig. S7b, ESI†) in the $FePS_3$/Pt heterostructure. Fig. S6b and S7b (ESI†) plot the angular dependence of R_{xx} at different magnetic field strengths (from 1 T to 9 T) at a fixed temperature of 2 K. The fitting equations for R_{xx} is given by

$$R_{xx}(\beta) = R_1 + R_{\mathrm{SMR}} \cos^2(2\beta), \quad (1)$$

$$R_{xx}(\gamma) = R_2 + R_{\mathrm{AMR}} \cos^2(2\gamma), \quad (2)$$

where R_1 and R_2 are the base resistance, R_{SMR} and R_{AMR} represent the SMR and AMR contributions, respectively, and γ and β are the field angles. The values of these parameters and SMR and AMR, which is calculated by $(R_{\mathrm{Max}} - R_{\mathrm{Min}})/R_{\mathrm{Min}}$ for all investigated fields are extracted and listed in Table S3 (ESI†). Fig. S6c and S7c (ESI†) display the angular dependence of R_{xx} at different temperatures (2 K to 80 K) at a fixed magnetic field strength (7 T). At lower temperatures (2 K and 10 K), R_{xx} exhibits strong angular dependence, indicating significant AMR. As the temperature increases, the amplitude of the angular variation in R_{xx} decreases, indicating a reduction in SMR and AMR.

In summary, we investigate the magnetic and electrical properties of $FePS_3$/Pt heterostructures, focusing on the AHE in the Pt layer. Despite $FePS_3$ being an antiferromagnetic insulator with no net magnetic moment, local magnetic moments are created at the interface. Facilitated by strong spin–orbit coupling, the MPE induces significant magnetization in Pt. Comprehensive measurements of the temperature, magnetic field, and angular dependence verify the occurrence of robust interfacial exchange interactions. The strong magnetization induction is attributed to Fe atom vacancies, which mediate the coupling and enhances these interactions. This finding suggests that combining defect engineering with interfacial phenomena such as the MPE makes an effective approach to creating net magnetization in non-magnetic metals in low-dimensional systems, paving the way for developing 2D heterostructures with both strong spin polarization and metallic conductivity for advanced spintronic devices.

Experimental methods

Material growth

High-quality bulk $FePS_3$ crystals were synthesized through the chemical vapor transport (CVT) method. Stoichiometric amounts of Fe, P, and S powders were mixed with a transport agent (I_2) in a sealed and evacuated quartz tube. The tube was placed for 7 days in a two-zone furnace with the source zone at 700 °C and the growth zone at 650 °C. The resulting $FePS_3$ crystals were then mechanically exfoliated into thin flakes using Scotch tape.

Compositional analysis

EDS measurements were performed using a Nova scanning electron microscope equipped with an EDS detector. The EDS analysis quantifies the composition ratios and possible Fe vacancies in the samples.

Device fabrication

The $FePS_3$/Pt heterostructures were fabricated using a mechanical exfoliation technique followed by sputtering deposition. The exfoliated $FePS_3$ flakes were transferred onto a Si/SiO_2 substrate using a dry transfer method assisted by polydimethylsiloxane (PDMS) stamps. A thin Pt layer was then deposited on the exfoliated $FePS_3$ flakes using magnetron sputtering under high-vacuum conditions. Optical microscopy and atomic force microscopy were used to confirm the thickness and quality of the transferred flakes and deposited Pt layers. Metal electrodes were patterned using electron beam lithography.

Characterization techniques

The structural characterization of the $FePS_3$ crystals was carried out using XRD with a Bruker D8 Advance diffractometer equipped with a Cu K_α X-ray source (λ = 1.5406 Å). Raman spectroscopy was performed using a Wetec Raman microscope with a 532-nm laser to verify the phase purity and crystallinity of the $FePS_3$ flakes. XPS was performed using a Kratos AMICUS XPS instrument equipped with a non-monochromated Al K_α ($h\nu$ = 1486.6 eV) X-ray source operated at 100 W with a pass energy of 75 eV. The base pressure of the analysis chamber was maintained below 5×10^{-7} Pa during data acquisition. For the high-resolution scan used to identify the peaks of Fe oxidation states, a dwell time of 500 ms per point was used. Atomic resolution HAADF-STEM images were obtained using FEI Titan Themes Cubed G2 300 (Cs Probe) TEM operated at 300 kV.

Magnetic and electrical measurements

The magnetic properties of the $FePS_3$/Pt heterostructures were measured using a Quantum Design superconducting quantum interference device (SQUID) magnetometer. The *M–H* curves were obtained at various temperatures ranging from 2 to 300 K. The magneto-transport behavior was measured using a Quantum Design physical property measurement system (PPMS). The longitudinal and transverse resistivity (R_{xx} and R_{xy}) were measured simultaneously using PPMS as a function of the magnetic field at different temperatures. The applied current was set to 100 μA. The magnetic field was applied perpendicular to the sample plane at the initial position (0°) that was rotated in *x–z* and *y–z* planes during angular dependence tests.

First-principles calculations

The first-principles calculations were conducted using the Vienna ab initio simulation package (VASP), employing the projector-augmented wave (PAW) method[59] along with the Perdew–Burke–Ernzerhof (PBE) exchange–correlation functional[60] for the simulations. A plane-wave energy cut-off of 450 eV was set for all calculations. For structural relaxations, a gamma-centered *k*-point grid with $ka > 30$ Å was used to sample the Brillouin zone, where *k* is the number of mesh points and *a* is the lattice constant. Specifically, a $3 \times 3 \times 1$ *k*-point grid was employed to achieve this density. A similar *k*-point mesh was used for all static runs. To avoid interactions between periodically repeated layers, a vacuum spacing of at least 20 Å was included along the *c*-axis. All atomic structures were relaxed until energy differences were below 10^{-6} eV, and the forces converged within 5×10^{-3} eV Å^{-1}. To accurately account for van der Waals interactions, the DFT-D3 method with Becke–Johnson damping function was utilized.[61,62] Additionally, spin polarization was enabled to account for magnetic effects.

Data availability

All data are presented in the main text or the ESI.†

Conflicts of interest

The authors declare that they have no competing interests.

Acknowledgements

This work was supported by King Abdullah University of Science and Technology (KAUST) Office of Sponsored Research under Award Nos ORA-CRG10-2021-4665 and ORA-CRG11-2022-5031. This research was undertaken with the resources from the Supercomputing Laboratory at KAUST in Saudi Arabia and the National Computational Infrastructure (NCI) in Australia.

References

1 X. Cai, T. Song, N. P. Wilson, G. Clark, M. He, X. Zhang, T. Taniguchi, K. Watanabe, W. Yao, D. Xiao, M. A. McGuire, D. H. Cobden and X. Xu, Atomically thin $CrCl_3$: an in-plane layered antiferromagnetic insulator, *Nano Lett.*, 2019, **19**, 3993–3998.
2 T. S. Ghiasi, A. A. Kaverzin, P. J. Blah and B. J. van Wees, Charge-to-spin conversion by the Rashba-Edelstein effect in two-dimensional van der Waals heterostructures up to room temperature, *Nano Lett.*, 2019, **19**, 5959–5966.
3 N. L. Nair, E. Maniv, C. John, S. Doyle, J. Orenstein and J. G. Analytis, Electrical switching in a magnetically intercalated transition metal dichalcogenide, *Nat. Mater.*, 2020, **19**, 153–157.

4 G. Chen, S. Qi, J. Liu, D. Chen, J. Wang, S. Yan, Y. Zhang, S. Cao, M. Lu, S. Tian, K. Chen, P. Yu, Z. Liu, X. C. Xie, J. Xiao, R. Shindou and J. H. Chen, Electrically switchable van der Waals magnon valves, *Nat. Commun.*, 2021, **12**, 6279.

5 D. L. Cortie, G. L. Causer, K. C. Rule, H. Fritzsche, W. Kreuzpaintner and F. Klose, Two-dimensional magnets: forgotten history and recent progress towards spintronic applications, *Adv. Funct. Mater.*, 2019, **30**, 1901414.

6 H. Li, S. Ruan and Y. J. Zeng, Intrinsic Van Der Waals Magnetic Materials from Bulk to the 2D Limit: New Frontiers of Spintronics, *Adv. Mater.*, 2019, **31**, e1900065.

7 M. A. Susner, M. Chyasnavichyus, M. A. McGuire, P. Ganesh and P. Maksymovych, Metal thio- and selenophosphates as multifunctional van der Waals layered materials, *Adv. Mater.*, 2017, **29**, 1602852.

8 F. Wang, T. A. Shifa, P. Yu, P. He, Y. Liu, F. Wang, Z. Wang, X. Zhan, X. Lou, F. Xia and J. He, New frontiers on van der Waals layered metal phosphorous trichalcogenides, *Adv. Funct. Mater.*, 2018, **28**, 1802151.

9 Y. Ma, Y. Yan, L. Luo, S. Pazos, C. Zhang, X. Lv, M. Chen, C. Liu, Y. Wang, A. Chen, Y. Li, D. Zheng, R. Lin, H. Algaidi, M. Sun, J. Z. Liu, S. Tu, H. N. Alshareef, C. Gong, M. Lanza, F. Xue and X. Zhang, High-performance van der Waals antiferroelectric $CuCrP_2S_6$-based memristors, *Nat. Commun.*, 2023, **14**, 7891.

10 C. Liu, S. Zhang, H. Hao, H. Algaidi, Y. Ma and X. X. Zhang, Magnetic skyrmions above room temperature in a van der Waals ferromagnet Fe_3GaTe_2, *Adv. Mater.*, 2024, **36**, e2311022.

11 H. Algaidi, C. Zhang, C. Liu, D. Zheng, Y. Ma, Y. Yuan and X. Zhang, Thickness-tunable magnetic and electronic transport properties of the quasi-two-dimensional van der Waals ferromagnet Co0.27TaS2 with disordered intercalation, *Phys. Rev. B*, 2023, **107**, 134406.

12 C. Zhang, C. Liu, S. Zhang, B. Zhou, C. Guan, Y. Ma, H. Algaidi, D. Zheng, Y. Li, X. He, J. Zhang, P. Li, Z. Hou, G. Yin, K. Liu, Y. Peng and X. X. Zhang, Magnetic skyrmions with unconventional helicity polarization in a van der Waals ferromagnet, *Adv. Mater.*, 2022, **34**, e2204163.

13 J. U. Lee, S. Lee, J. H. Ryoo, S. Kang, T. Y. Kim, P. Kim, C. H. Park, J. G. Park and H. Cheong, Ising-type magnetic ordering in atomically thin $FePS_3$, *Nano Lett.*, 2016, **16**, 7433–7438.

14 F. Feringa, G. E. W. Bauer and B. J. van Wees, Observation of magnetization surface textures of the van der Waals antiferromagnet $FePS_3$ by spin Hall magnetoresistance, *Phys. Rev. B*, 2022, **105**, 214408.

15 K. Z. Du, X. Z. Wang, Y. Liu, P. Hu, M. I. Utama, C. K. Gan, Q. Xiong and C. Kloc, Weak van der Waals stacking, wide-range band gap, and Raman study on ultrathin layers of metal phosphorus trichalcogenides, *ACS Nano*, 2016, **10**, 1738–1743.

16 A. R. Wildes, D. Lançon, M. K. Chan, F. Weickert, N. Harrison, V. Simonet, M. E. Zhitomirsky, M. V. Gvozdikova, T. Ziman and H. M. Rønnow, High field magnetization of $FePS_3$, *Phys. Rev. B*, 2020, **101**, 024415.

17 F. Feringa, J. M. Vink and B. J. van Wees, Spin Nernst magnetoresistance for magnetization study of $FePS_3$, *Phys. Rev. B*, 2023, **107**, 094428.

18 T. Su, M. Lohmann, J. X. Li, Y. D. Xu, B. Niu, M. Alghamdi, H. D. Zhou, Y. T. Cui, R. Cheng, T. Taniguchi, K. Watanabe and J. Shi, Current-induced CrI3 surface spin-flop transition probed by proximity magnetoresistance in Pt, *2D Mater.*, 2020, **7**, 045006.

19 C. Ye, X. Xie, W. Lv, K. Huang, A. J. Yang, S. Jiang, X. Liu, D. Zhu, X. Qiu, M. Tong, T. Zhou, C. H. Hsu, G. Chang, H. Lin, P. Li, K. Yang, Z. Wang, T. Jiang and X. Renshaw Wang, Nonreciprocal transport in a bilayer of $MnBi_2Te_4$ and Pt, *Nano Lett.*, 2022, **22**, 1366–1373.

20 M. Lohmann, T. Su, B. Niu, Y. Hou, M. Alghamdi, M. Aldosary, W. Xing, J. Zhong, S. Jia, W. Han, R. Wu, Y. T. Cui and J. Shi, Probing magnetism in insulating $Cr_2Ge_2Te_6$ by induced anomalous Hall effect in Pt, *Nano Lett.*, 2019, **19**, 2397–2403.

21 C. Tang, Z. Zhang, S. Lai, Q. Tan and W. B. Gao, Magnetic proximity effect in graphene/CrB_3 van der Waals Heterostructures, *Adv. Mater.*, 2020, **32**, e1908498.

22 Y. Zhang, W. Wang, M. Huang, P. Liu, G. Hu, C. Feng, X. Lei, M. Gu, H. Yang, K. Liu, B. Xiang and Y. Lu, $MnPS_3$ spin-flop transition-induced anomalous Hall effect in graphite flake via van der Waals proximity coupling, *Nanoscale*, 2020, **12**, 23266–23273.

23 W. Tang, D. Zhao, X. Weng, K. Wu, Z. Yang, C. Kang, Y. Sun, W.-C. Jiang, H. Liang, C. Wang and Y.-J. Zeng, Unveiling magnetism in individual $CuCrP_2S_6$ flakes by magnetic proximity effect, *Appl. Phys. Rev.*, 2023, **10**, 031404.

24 S. Ding, Y. Peng, M. Xue, Z. Liu, Z. Liang, W. Yang, Y. Sun, J. Zhao, C. Wang, S. Liu, J. Han and J. Yang, Magnetic phase diagram of $CrPS_4$ and its exchange interaction in contact with NiFe, *J. Phys.: Condens. Matter*, 2020, **32**, 405804.

25 T. Zhang, Y. Zhang, M. Huang, B. Li, Y. Sun, Z. Qu, X. Duan, C. Jiang and S. Yang, Tuning the exchange bias effect in 2D van der Waals ferro-/antiferromagnetic Fe_3GeTe_2/CrOCl heterostructures, *Adv. Sci.*, 2022, **9**, e2105483.

26 W. Sun, W. Wang, D. Chen, Z. Cheng and Y. Wang, Valence mediated tunable magnetism and electronic properties by ferroelectric polarization switching in 2D FeI_2/In_2Se_3 van der Waals heterostructures, *Nanoscale*, 2019, **11**, 9931–9936.

27 H. Yang, M. Gobbi, F. Herling, V. T. Pham, F. Calavalle, B. Martín-García, A. Fert, L. E. Hueso and F. L. Casanova, A seamless graphene spin valve based on proximity to van der Waals magnet $Cr_2Ge_2Te_6$, *Nat. Electron.*, 2024, 15–23.

28 L. Pan, A. Grutter, P. Zhang, X. Che, T. Nozaki, A. Stern, M. Street, B. Zhang, B. Casas, Q. L. He, E. S. Choi, S. M. Disseler, D. A. Gilbert, G. Yin, Q. Shao, P. Deng, Y. Wu, X. Liu, X. Kou, S. Masashi, X. Han, C. Binek, S. Chambers, J. Xia and K. L. Wang, Observation of quantum anomalous Hall effect and exchange interaction in topological insulator/antiferromagnet heterostructure, *Adv. Mater.*, 2020, **32**, e2001460.

29 Y. Zhao, H. Huang, Z. Zhang, L. Wang, Y. Wu, C. Liu, J. Zhang, X. Zheng, S. Zhou and S. Wang, Magnetic

proximity effect on the spin-valley coupling in two-dimensional $Cr_2Ge_2Te_6$/2H-TMD van der Waals heterostructures, *J. Appl. Phys.*, 2024, **135**, 153901.

30 B. Huang, M. A. McGuire, A. F. May, D. Xiao, P. Jarillo-Herrero and X. D. Xu, Emergent phenomena and proximity effects in two-dimensional magnets and heterostructures, *Nat. Mater.*, 2020, **19**, 1276–1289.

31 K. Zollner and J. Fabian, Proximity effects in graphene on monolayers of transition-metal phosphorus trichalcogenides MPX_3 (M: Mn, Fe, Ni, Co, and X: S, Se), *Phys. Rev. B*, 2022, **106**, 035137.

32 D. Zhong, K. L. Seyler, X. Linpeng, N. P. Wilson, T. Taniguchi, K. Watanabe, M. A. McGuire, K. C. Fu, D. Xiao, W. Yao and X. Xu, Layer-resolved magnetic proximity effect in van der Waals heterostructures, *Nat. Nanotechnol.*, 2020, **15**, 187–191.

33 T. P. Lyons, D. Gillard, A. Molina-Sanchez, A. Misra, F. Withers, P. S. Keatley, A. Kozikov, T. Taniguchi, K. Watanabe, K. S. Novoselov, J. Fernandez-Rossier and A. I. Tartakovskii, Interplay between spin proximity effect and charge-dependent exciton dynamics in $MoSe_2$/$CrBr_3$ van der Waals heterostructures, *Nat. Commun.*, 2020, **11**, 6021.

34 J. Li, M. Rashetnia, M. Lohmann, J. Koo, Y. Xu, X. Zhang, K. Watanabe, T. Taniguchi, S. Jia, X. Chen, B. Yan, Y. T. Cui and J. Shi, Proximity-magnetized quantum spin Hall insulator: monolayer 1 T' WTe_2/$Cr_2Ge_2Te_6$, *Nat. Commun.*, 2022, **13**, 5134.

35 Z. Wang, C. Tang, R. Sachs, Y. Barlas and J. Shi, Proximity-induced ferromagnetism in graphene revealed by the anomalous Hall effect, *Phys. Rev. Lett.*, 2015, **114**, 016603.

36 M. Asa, C. Rinaldi, R. Pazzocco, D. Petti, E. Albisetti, R. Bertacco and M. Cantoni, Electrical readout of the antiferromagnetic state of IrMn through anomalous Hall effect, *J. Appl. Phys.*, 2020, **128**, 053904.

37 A. E. Llacsahuanga Allcca, X. C. Pan, I. Miotkowski, K. Tanigaki and Y. P. Chen, Gate-tunable anomalous Hall effect in stacked van der Waals ferromagnetic insulator-topological insulator heterostructures, *Nano Lett.*, 2022, **22**, 8130–8136.

38 H. Yan, Z. Feng, P. Qin, X. Zhou, H. Guo, X. Wang, H. Chen, X. Zhang, H. Wu and C. Jiang, Electric-field-controlled antiferromagnetic spintronic devices, *Adv. Mater.*, 2020, **32**, 1905603.

39 H. Xu, S. Wang, J. Ouyang, X. He, H. Chen, Y. Li, Y. Liu, R. Chen and J. Yang, Surface modification of multilayer $FePS_3$ by Ga ion irradiation, *Sci. Rep.*, 2019, **9**, 15219.

40 H. B. Vasili, M. Gamino, J. Gazquez, F. Sanchez, M. Valvidares, P. Gargiani, E. Pellegrin and J. Fontcuberta, Magnetoresistance in hybrid Pt/$CoFe_2O_4$ bilayers controlled by competing spin accumulation and interfacial chemical reconstruction, *ACS Appl. Mater. Interfaces*, 2018, **10**, 12031–12041.

41 A. Manchon and A. Belabbes, Spin-orbitronics at transition metal interfaces, *Solid State Phys.*, 2017, **68**, 1–89.

42 K. Kurosawa, S. Saito and Y. Yamaguchi, Neutron diffraction study on $MnPS_3$ and $FePS_3$, *J. Phys. Soc. Jpn.*, 1983, **52**, 3919–3926.

43 Z. Shi, H.-Y. Jiang, S.-M. Zhou, Y.-L. Hou, Q.-L. Ye and M. Su Si, Effect of band filling on anomalous Hall conductivity and magneto-crystalline anisotropy in NiFe epitaxial thin films, *AIP Adv.*, 2016, **6**, 015101.

44 M. Amirabbasi and P. Kratzer, Effect of biquadratic magnetic exchange interaction in the 2D antiferromagnets MPS_3 (M = Mn,Fe,Co,Ni), *Phys. Rev. Mater.*, 2024, **8**, 084005.

45 B. L. Chittari, Y. Park, D. Lee, M. Han, A. H. MacDonald, E. Hwang and J. Jung, Electronic and magnetic properties of single-layerMPX3metal phosphorous trichalcogenides, *Phys. Rev. B*, 2016, **94**, 184428.

46 S. Maity, D. Dey, A. Ghosh, S. Masanta, B. K. De, H. S. Kunwar, B. Das, T. Kundu, M. Palit, S. Bera, K. Dolui, K. Watanabe, T. Taniguchi, L. Yu, A. Taraphder and S. Datta, Manipulating spin-lattice coupling in layered magnetic topological insulator heterostructure via interface engineering, *Adv. Funct. Mater.*, 2024, **34**, 2402544.

47 F. Haddadi, E. Linscott, I. Timrov, N. Marzari and M. Gibertini, On-site and intersite Hubbard corrections in magnetic monolayers: The case of $FePS_3$ and CrI_3, *Phys. Rev. Mater.*, 2024, **8**, 014007.

48 M. Amirabbasi and P. Kratzer, Orbital and magnetic ordering in single-layer $FePS_3$: A DFT+U study, *Phys. Rev. B*, 2023, **107**, 024401.

49 M. Hong, L. Dai, H. Hu and C. Li, Structural, ferroelectric, and electronic transitions in the van der Waals multiferroic material $CuCrP_2S_6$ under high temperature and high pressure, *Phys. Rev. B*, 2024, **110**, 144103.

50 K. Yang, Y. Ning, Y. Zhou, D. Lu, Y. Ma, L. Liu, S. Pu and H. Wu, Understanding the Ising zigzag antiferromagnetism of $FePS_3$ and $FePSe_3$ monolayers, *Phys. Rev. B*, 2024, **110**, 024427.

51 Y. Ou, X. Li, J. Kopaczek, A. Davis, G. Jackson, M. Sayyad, F. Liu and S. A. Tongay, The hard ferromagnetism in $FePS_3$ induced by non-magnetic molecular intercalation, *Adv. Phys. Res.*, 2024, 2400101.

52 T. Ikeda, M. Tsunoda, M. Oogane, S. Oh, T. Morita and Y. Ando, Anomalous Hall effect in polycrystalline Mn_3Sn thin films, *Appl. Phys. Lett.*, 2018, **113**, 222405.

53 X. Zhou, L. Ma, Z. Shi, W. J. Fan, J.-G. Zheng, R. F. L. Evans and S. M. Zhou, Magnetotransport in metal/insulating-ferromagnet heterostructures: Spin Hall magnetoresistance or magnetic proximity effect, *Phys. Rev. B: Condens. Matter Mater. Phys.*, 2015, **92**, 060402.

54 X. Zhou, L. Ma, Z. Shi, G. Y. Guo, J. Hu, R. Q. Wu and S. M. Zhou, Tuning magnetotransport in PdPt/$Y_3Fe_5O_{12}$: Effects of magnetic proximity and spin-orbit coupling, *Appl. Phys. Lett.*, 2014, **105**, 012408.

55 Q. Shao, A. Grutter, Y. Liu, G. Yu, C.-Y. Yang, D. A. Gilbert, E. Arenholz, P. Shafer, X. Che, C. Tang, M. Aldosary, A. Navabi, Q. L. He, B. J. Kirby, J. Shi and K. L. Wang, Exploring interfacial exchange coupling and sublattice effect in heavy metal/ferrimagnetic insulator heterostructures using Hall measurements, x-ray magnetic circular dichroism, and neutron reflectometry, *Phys. Rev. B*, 2019, **99**, 104401.

56 C. Wang, C. H. Chang, A. Herklotz, C. Chen, F. Ganss, U. Kentsch, D. Chen, X. Gao, Y. J. Zeng, O. Hellwig, M. Helm, S. Gemming, Y. H. Chu and S. Zhou, Topological Hall effect in single thick $SrRuO_3$ layers induced by defect engineering, *Adv. Electron. Mater.*, 2020, **6**, 2000184.
57 E. Vilanova Vidal, H. Schneider and G. Jakob, Influence of disorder on anomalous Hall effect for Heusler compounds, *Phys. Rev. B:Condens. Matter Mater. Phys.*, 2011, **83**, 174410.
58 J. Mukherjee, T. S. Suraj, H. Basumatary, K. Sethupathi and K. V. Raman, Sign reversal of anomalous Hall conductivity and magnetoresistance in cubic noncollinear antiferromagnet Mn_3Pt thin films, *Phys. Rev. Mater.*, 2021, **5**, 014201.
59 G. Kresse and D. Joubert, From ultrasoft pseudopotentials to the projector augmented-wave method, *Phys. Rev. B*, 1999, **59**, 1758.
60 J. P. Perdew, K. Burke and M. Ernzerhof, Generalized gradient approximation made simple, *Phys. Rev. Lett.*, 1996, **77**, 3865.
61 S. Grimme, J. Antony, S. Ehrlich and H. Krieg, A consistent and accurate ab initio parametrization of density functional dispersion correction (DFT-D) for the 94 elements H-Pu, *J. Chem. Phys.*, 2010, **132**, 154104.
62 S. Grimme, S. Ehrlich and L. Goerigk, Effect of the damping function in dispersion corrected density functional theory, *J. Comput. Chem.*, 2011, **32**, 1456–1465.